Computational algorithm for evaluating gravitational and inertial loads acting on an industrial robot for palletizing operations

Roxana-Mariana Nechita* , Cozmin Cristoiu , Mihai Mărgăritescu

Abstract. *This paper introduces a computational algorithm designed to calculate the gravitational and inertial loads affecting a four-axis numerically controlled (NC) industrial robot (IR) used in palletizing operations. The methodology includes the development of precise calculation models that account for the dynamic interactions between the robot's mechanical components and its operational environment. These models enable the accurate determination of load distributions and stresses on each axis, which are critical for optimizing the robot's performance and ensuring reliable operation under various loading conditions. The algorithm can be applied to the optimization and refinement of existing robotic systems, as well as to the design of new robots tailored for specific industrial applications.*

Keywords*: industrial robot, optimal structure, calculus algorithm, palletizing, unfavorable position.*

1. Introduction

Palletizing is the process of arranging objects into uniform horizontal layers and multiple vertical layers on standardized transport supports known as pallets. This process involves handling various types of objects, either individually or in groups, by industrial robots or automated palletizing machines. The application underpinning this study (Figure 1) is a robotic cell designed for palletizing prismatic objects, featuring a single entry and exit point, integrating an IR with a four-axis NC articulated arm. Within this cell, a pallet is introduced from a stack into the cell via a roller conveyor. After the pallet is evacuated from the cell, another pallet is brought in to continue the palletizing process. On the input conveyor, products to be handled are transported. These products consist of prismatic cardboard boxes, each containing six 750 ml bottles of wine. During transport, the products are inspected by two measurement sensors positioned above the conveyor to identify any defects. If defective products are identified, they are removed

from the flow through a system that marks the end of the objects' path on the roller conveyor-defective items are allowed to fall into a container located at the end of the conveyor. Conforming products are then brought into the workspace of the IR. The IR picks up the boxes that have reached the end of the conveyor and positions them optimally on the pallet according to a predefined algorithm. When the pallet, along with the accumulated load, reaches the maximum allowable height, it is evacuated from the cell via the conveyor. The loaded pallet is then taken by a human operator using a forklift to proceed to the next stage of the logistic process.
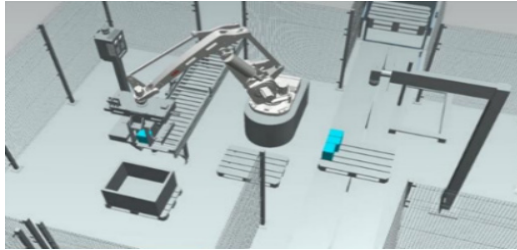
Figure 1. Robotic palletizing cell

1.1. Robot equivalence

Palletizing operations can be performed using robots with articulated arm or gantry architecture, which are commonly equipped with 5 or 6 degrees of freedom. In the case of IR with articulated arms, there is an option to use dedicated robots specifically tailored for palletizing operations. These dedicated articulated-arm robots typically feature 5 rotational degrees of freedom but are NC through only 4 axes. The distinctive feature of these dedicated robots lies in a specially designed mechanical system that enables pitch orientation movement [1]. This system ensures the permanent vertical alignment of the roll axis, regardless of the angular positions of the articulated arm segments. Implementing such a system involves the use of two closed-loop kinematic chain subsystems and a unique coupling design that facilitates pitch orientation movements [2].

The ABB IRB 660=180/3.15 [3] is an articulated arm robot with a closed kinematic chain designed for palletizing. Its workspace is spherically articulated with a radius of 3150 mm. These structural and functional parameters justify the capabilities of the robot in the following aspects:
- Bearing load capacity:

The weight of a single product (a crate containing 6 bottles of 0.75l of wine with cardboard separators) is :

$$0.6\ kg\ (cardboard) + 4.5\ kg\ (wine) + 2.622\ kg\ (glass) \atop + 0.012\ kg\ (cork) = 7.7 kg \qquad (1)$$

The unfavorable position (Figure 2) of the IR in the application captures the handling of 3 boxes, weighing 23.1kg. The robot can handle heavy loads in palletizing applications. In an unfavorable situation, it can handle up to 93.541 kg, including a 70.441 kg prism object handling effector.
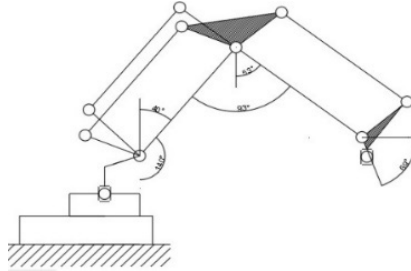
Figure 2. The structural kinematic diagram of the robot
in the unfavorable position.

The maximum length required to move in the unfavorable position is 1859.69 mm. The robot has an articulated spherical workspace with a radius of 3150 mm, which is compatible with the cell requirements shown in Figure 1.

The robot shall be accurate and repeatable in its operations. This includes the volumetrically orderly arrangement in the horizontal and vertical plane (layers with homogeneous heights) and the accurate handling of prismatic bodies for pallet assembly. Technical specifications of ABB IRB 660=180/3.15 [3] are: maximum payload: 180 kg; nc axis number: 4; controller type: irc5 single/dual; cabinet maximum reach: 3.15 m and robot weight: 1650 kg. Thus, the ABB IRB 660=180/3.15 robot is optimized for palletizing tasks due to its robust structure, generous workspace and ability to handle heavy loads in a precise and repeatable manner.

2. Sequence of calculation stages

Concerning the order of the major computational steps for the design of the overall IR assembly, in addition to the aspects mentioned above, it is crucial to follow the following fundamental principles to perform the necessary computations for the overall IR's assembly [4]. In the preliminary stages of calculation, it is essential to establish the input data taking into account the specificity of the application in which the IR will be integrated and the functional characteristics of the previously selected reference IR model. These inputs include the IR-specific design parameters and the maximum limits of velocities and motions on the numerically controlled axes of the IR. In order to start the design of a rotational axis in a robot with n degrees of freedom (DOF), all constructive elements for each partial assembly corresponding to the NC axes (k + 1 to n) must be determined based on the

previous design and calculation steps [5]. Next, it is essential to correctly identify and locate the loads in the design scheme, including specific forces and moments.

In order to carefully follow these issues, the main computational steps for the overall IR assembly design are realized in the following sequences: development of the computational scheme for the design of the IR; identifying the location of mass in each major partial assembly of the RI;identification of the general distribution of gravitational and inertial loads applied on the overall robot structure, using the most appropriate configuration; determine the calculation for each IR's partial assembly; distribution of spatial loads on the computational centers over the entire robot structure; calculation of the results of reduced forces and moments (F, M); distribution of the forces and moments (F, M) previously applied on each IR joint, applied on the bearings or guides of the movable elements and components included in the kinematic/ driving chain responsible for the rotational/linear motion of each IR movable element. The computational steps for obtaining the final usable results, including the final selection of the standardized IR's part assemblies, include: preliminary dimensioning, choosing, and ultimate validation of mechanical components; preliminary assessment, choice, and validation of servomotors and position/speed sensors employed across each NC axis; final verification of the selected servomotors and encoder systems used for continuous adjustment of the servomotor parameters on each NC axis; evaluating the performance of each individual sub-assembly within the robot; assessing the overall performance of the complete robot assembly. These steps provide a detailed methodology for the complete design and evaluation of the IR, ensuring compliance with specific design and functionality requirements in various industrial applications.

### 3. Determination of distribution for gravitational and inertial loads

In this calculation stage, using the established calculation scheme and the optimal configuration for designing partial assemblies, the following key aspects are determined:

• The gravitational loads (Gi) specific to each structural element of the IR and each partial subsystem, along with their spatial distribution across the entire IR assembly (Figure 3).

a.   b.
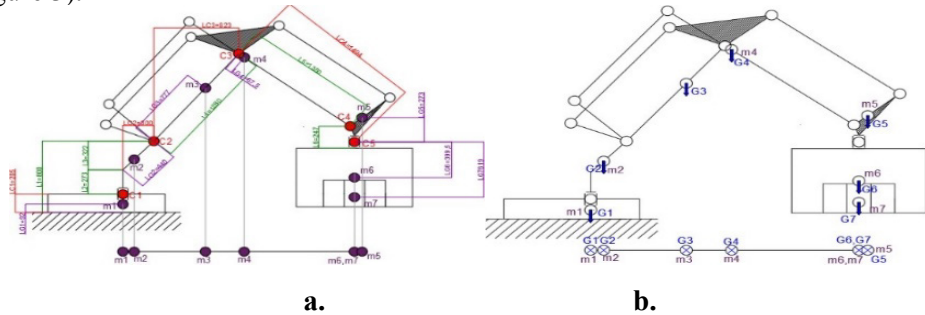
Figure 3. a. Locating calculation centers and mass centers on the kinematic diagram; **b.** Representation of gravitational forces on the kinematic diagram.

• The inertial forces generated by the mass of the IR's mobile elements and their manner of distribution in the rotational joints (Figure 4).

a. **b.**

c.
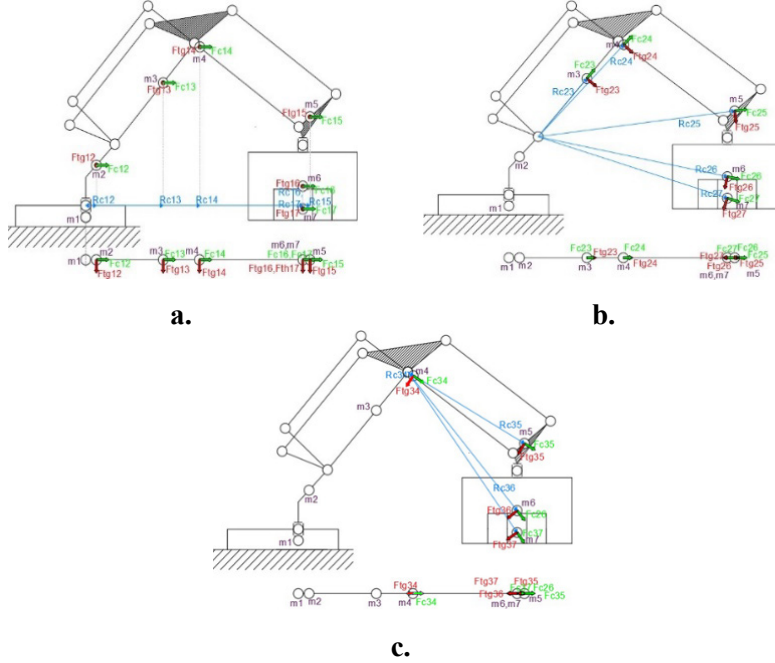
Figure 4.a. Representation of centrifugal forces, tangential forces, and kinematic radii on the kinematic calculation scheme for the possibility of motion in coupling 1;
b. Representation of centrifugal forces, tangential forces, and kinematic radii on the kinematic calculation scheme for the possibility of motion in coupling 2;
c. Representation of centrifugal forces, tangential forces, and kinematic radii on the kinematic calculation scheme for the possibility of motion in coupling 3.

• The principal moments of inertia of the structural elements/partial assemblies of the IR caused by rotational movements in each major/active joint.

To determine the spatial distribution of the gravitational and inertial loads considered in the design of the IR's NC axes, numerical evaluation and detailed graphical representation are employed on the previously developed calculation scheme: gravitational forces and inertial forces acting at characteristic mass centers of the IR's structural elements. In graphical representation on the calculation scheme, gravitational and inertial force loads are applied only at their respective centers, while inertial moments are applied around the rotation axes that generate them. Additionally, for each type of inertial force/moment of inertia, the specific direction and mode of action are determined, taking into account the movements of the elements and the timing of the inertial load [6].

The known input data for determining the specific radii and angles are presented in Table 1.

Table 1. Input data.

LC_n[mm]	LG_n[mm]	$L_n = 800$ [mm]
$LC_1 = 205$	$LG_1 = 92$	$L_1 = 800$
$LC_2 = 300$	$LG_2 = 161$	$L_2 = 273$
$LC_3 = 823$	$LG_3 = 777$	$L_3 = 322$
$LC_4 = 1494$	$LG_4 = 67.5$	$L_4 = 1280$
	$LG_5 = 273$	$L_5 = 1350$
	$LG_6 = 399.5$	
	$LG_7 = 619$	

For couple 1, the radii will be determined as follows:

a.   b.   c.

d.   e.
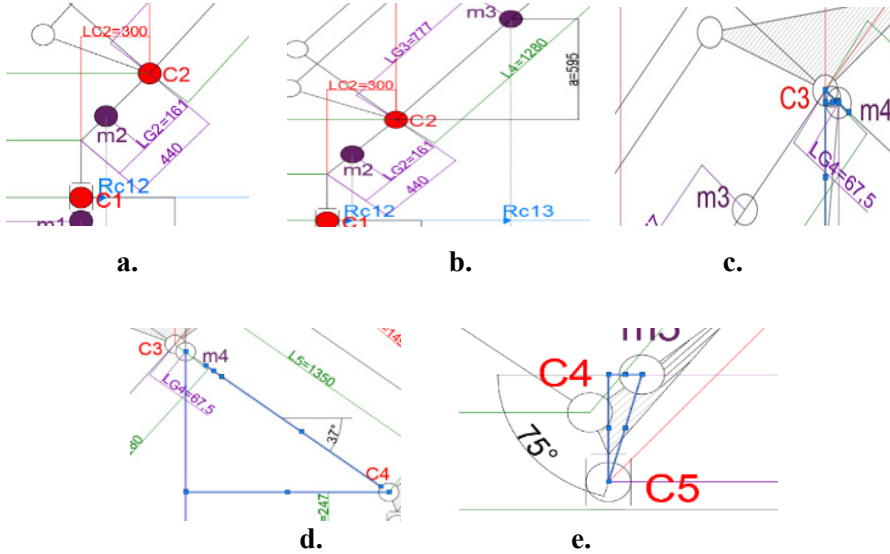
Figure 5. Sketches used to determine Rc_{1n}: **a.** triangle for Rc_{13}; **b.** triangle for Rc_{14}; **c.** Triangle for Rc_{15}; **d.** Triangle for Rc_{16}; **e.** triangle for Rc_{17}.

To determine Rc_{12}, we will use the similarity of triangles, using the triangle (Figure 5) a with sides: $LC_2 = 300\ mm$, $L_3 = 322\ mm$ and $LG_2 = 161\ mm$.

$$\frac{a}{L_3} = \frac{LG_2}{b} = \frac{Rc_{12}}{LC_2} \qquad (2)$$

20

$$Rc_{12} = \frac{LG_2 \cdot LC_2}{b} \tag{3}$$

To determine Rc_{13}, we will use the triangle (Figure 5.a) with sides $LG_3 + LG_2$, Zm_3, and Rc_{13}-Rc_{12}:

$$Zm_3 - 800 \ mm = 595 \ mm \tag{4}$$
$$Rc_{13} = \sqrt{(LG_3 + 440)^2 - (a + L_3)^2} \tag{5}$$

We will construct the following right triangle (Figure 5.b) to find Rc_{14} using the Law of Sines.

$$\frac{67.5 \ mm}{sin \ (90°)} = 67.5 \ mm \tag{6}$$
$$67.5 \ mm = 2R \tag{7}$$
$$2R \cdot sin(53°) = 53.91 \ mm \tag{8}$$
$$Rc_{14} = 53.91 \ mm + LC_3 + LC_3 \tag{9}$$

Use the right triangle in Figure 5.c. to find the projection of m_4-C_4, using the Sine Theorem:

$$\frac{L5 - LG4}{sin \ (90°)} = \frac{1350 - 67.5}{sin \ (90°)} \tag{10}$$
$$Rc_{14} = 53.91 \ mm + 823 \ mm + 300 \ mm \tag{11}$$
$$Rc_{15} = Rc_{14} + 1024.25 \ mm + 115{,}58 \ mm \tag{12}$$

Use the following right triangle (Figure 5.e) to deduce $Rc_{16} = Rc_{17}$, using the Sine Theorem:

$$\frac{LG_5}{sin \ (75°)} = \frac{247}{sin \ (75°)} \tag{13}$$
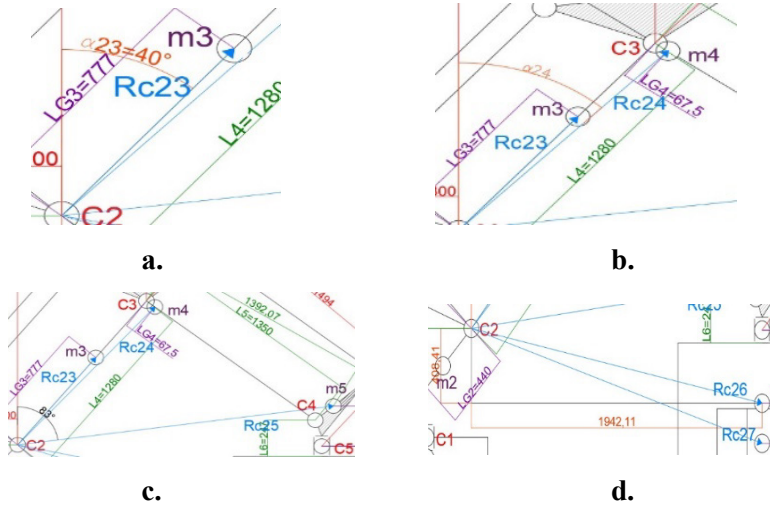$$\frac{C_4\_m_5}{sin \ (15°)} = 283.26 \ mm \tag{14}$$
$$Rc_{16} = Rc_{17} \tag{15}$$
$$Rc_{16} = Rc_{15} - 74.4 \ mm \tag{16}$$

Thus, Rc_{1n} are known (Table 2).

Table 2. The values of $Rc_{1n}[mm]$

Rc_{12}	Rc_{13}	Rc_{14}	Rc_{15}	Rc_{16}	Rc_{17}
109.05	799.45	1176.68	2316.51	2242.11	2242.11

For couple 2, the radii will be determined as follows:

Figure 6. Sketches used to determine the Rc_{2n}: **a.** The triangle used to determine Rc_{23}, α_{23}; **b.** The triangle used to determine Rc_{24}, α_{24}; **c.** The triangle used to determine Rc_{25}, α_{25}; **d.** The triangle used to determine $Rc_{26}, \alpha_{26}, Rc_{27}, \alpha_{27}$.

Rc_{23} corresponds to LG_3 (Figure 6.a).

α_{23} corresponds to the angle of the unfavorable position.

To determine Rc_{24}, we will use the triangle (Figure 6.b) with sides Rc_{24}, L_4, and LG_4, applying the Cosine Theorem as follows:

$$Rc_{24} = \sqrt{(LG_4{}^2 + LG_4{}^2 - 2 \cdot LG_4 \cdot L_4 \cdot \cos{(93°)})}mm \tag{17}$$

To determine the angle α_{24}, the angle formed between Rc_{23} and Rc_{24} will be used, which will be found by applying the Sine Theorem in the triangle (Figure 6.b) with sides Rc_{24}, L_4, and LG_4.

$$\frac{Rc_{24}}{\sin{(93°)}} = \frac{LG_4}{\sin{b}} \tag{18}$$

$$sin^{-1}(0.05) = 3° \tag{19}$$

$$\alpha_{24} = \alpha_{23} + 3° \tag{20}$$

To determine Rc_{25}, the Sine Theorem will be applied (Figure 6.c):

$$Rc_{25} = \sqrt{(1392.07^2 + 1280^2 - 2 \cdot 1392.07 \cdot 1280 \cdot \cos{(99°)})}mm \tag{21}$$

To determine , α_{25}, the Sine Theorem will be applied (Figure 6.c):

$$\frac{Rc_{25}}{\sin(99°)} = \frac{2033.77 \ mm}{\sin(99°)} \tag{22}$$

$$\frac{1392.07 \ mm}{\sin a} = 2059.36 \ mm \tag{23}$$

$$\sin a = \frac{1392.07}{2059.36} \ mm \tag{24}$$

$$\alpha_{25} = (43 + Rc_{23})° \tag{25}$$

To determine Rc26, the Pythagorean Theorem will be applied (Figure 6.d):

$$Rc_{26} = \sqrt{1942.11^2 + 408.41^2} \ mm \tag{26}$$

$$Rc_{27} = \sqrt{1942.11^2 + 627.91^2} \ mm \tag{27}$$

$$\frac{1984.59}{\sin(90°)} = \frac{1942.11 \ mm}{\sin b} \tag{28}$$

$$\sin b = \frac{1942.11}{1984.59} \ mm \tag{29}$$

$$\frac{2041.1}{\sin(90°)} = \frac{1942.11}{\sin c} \tag{30}$$

$$\alpha_{27} = 180° - 72° \tag{31}$$

Thus, Rc_{2n} (Table 3) and α_{2n} (Table 4) are known.

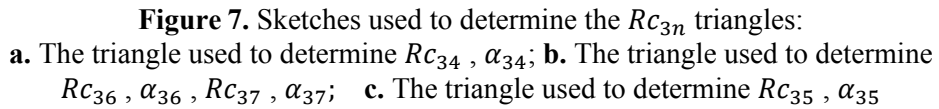**Table 3.** The values of $Rc_{2n}[mm]$

Rc_{23}	Rc_{24}	Rc_{25}	Rc_{26}	Rc_{27}
777	1285.3	2033.77	1984.59	2041.1

Table 4. The values of α_{2n}

α_{2n}	α_{2n}	α_{2n}	α_{2n}	α_{2n}
40°	43°	83°	102°	108°

For coupling 3, the radii will be determined as follows:

Figure 7. Sketches used to determine the Rc_{3n} triangles:
a. The triangle used to determine Rc_{34} , α_{34}; **b.** The triangle used to determine Rc_{36} , α_{36} , Rc_{37} , α_{37};   **c.** The triangle used to determine Rc_{35} , α_{35}

In the case of Rc_{34}, the procedure will be as follows:

$$Rc_{34} \text{ corresponds to } LG_4 = Rc_{34} \tag{32}$$
$$Rc_{34} = 67.5 \ mm \tag{33}$$

α34 corresponds to the angle of the unfavorable position (Figure 7.a)

To determine R35, the Pythagorean Theorem will be used (Figure 7.b) as follows:

$$Rc_{15} - Rc_{14} + 53.91 = 1193.74 \ mm \tag{34}$$
$$Rc_{35} = \sqrt{(1193.74^2 + 716.13^2} \ mm \tag{35}$$

The Sine Theorem will be applied (Figure 7.c) to find the value of the angle α_{35}:

$$\frac{Rc_{35}}{sin \ (90)} = \frac{1392.07 \ mm}{sin \ (90°)} \tag{36}$$
$$sin \ \alpha_{35} = \frac{716.13}{1392.07} mm \tag{37}$$

To determine Rc_{36} and Rc_{37}, the Pythagorean theorem will be used first (Figure 7.b), followed by applying the Sine theorem to find the angles α_{36} and α_{37}.

24

$$Rc_{36} = \sqrt{(1119.34^2 + 1388.95^2} \ mm \qquad (38)$$

$$Rc_{37} = \sqrt{(1119.34^2 + 1608.45^2} \qquad (39)$$

$$\frac{Rc_{36}}{sin\ (90)} = \frac{1783.85\ mm}{sin\ (90°)} \qquad (40)$$

$$\frac{1388.95\ mm}{sin\ \alpha_{36}} = 1783.85\ mm \qquad (41)$$

$$\frac{Rc_{37}}{sin\ (90)} = \frac{1959.6\ mm}{sin\ (90°)} \qquad (42)$$

Thus, Rc_{2n} (Table 5) and α_{2n} (Table 6) are known.

Table 5. The values of $Rc_{2n}[mm]$

Rc_{34}	Rc_{35}	Rc_{36}	Rc_{37}
67.5	1303.07	1783.85	1959.6

Table 6. The values of α_{2n}

α_{2n}	α_{2n}	α_{2n}	α_{2n}
37°	31°	51°	55°

To determine the values of the gravitational forces acting on the robot in the actuation of couplings 1, 2 and 3 the following formula will be used: $G_n = m_n * g$ [N], where $g = 9.81\frac{m}{s^2}$ (Table 7).

Table 7. The values of $G_n[N]$

G_1	G_2	G_3	G_4	G_5	G_6	G_7
3979.12	5979.24	3040.29	2330.89	873.95	686.7	226.61

The angular velocities ω_n of axes 1, 2 and 3 are as follows:

$$\omega_1 = 130°/s = 2.2689\ rad/s \qquad (43)$$
$$\omega_2 = 130°/s = 2.2689\ rad/s \qquad (44)$$
$$\omega_3 = 130°/s = 2.2689\ rad/s \qquad (45)$$

Angular accelerations ε_n, will be determined (Table 8), knowing that $t_{acc/fr} = 0.5s$:

$$\varepsilon_n = \frac{\omega_n}{t_{acc/fr}} \qquad (46)$$

Table 8. The values of $\varepsilon_n[rad/s^2]$

ε_1	ε_2	ε_3
4.5378	4.5378	4.5378

The angular accelerations, centrifugal forces, and tangential forces caused by the motion in couple n are as follows:

$$atg_{n,n+a} = \varepsilon_n \cdot Rc_{n,n+a} \cdot 10^{-3} \qquad (47)$$
$$Fcf_{n,n+a} = m_{n+a} \cdot Rc_{12} \cdot 10^{-3} \qquad (48)$$
$$Ftg_{n,n+a} = m_2 \cdot atg_{n,n+a} \qquad (49)$$

The following were thus determined: $atg_{n,n+a}, Fcf_{n,n+a}, Ftg_{n,n+a}$ (Table 9).

Table 9. The values of $atg_{n,n+a}, Fcf_{n,n+a}, Ftg_{n,n+a}$

$atg_{n,n+a}[m/s^2]$	$Fcf_{n,n+a}[N]$	$Ftg_{n,n+a}[N]$
$atg_{12} = 0.49$	$Fcf_{12} = 66.63$	$Ftg_{12} = 302.35$
$atg_{13} = 3.62$	$Fcf_{13} = 247.76$	$Ftg_{13} = 1124.76$
$atg_{14} = 5.33$	$Fcf_{14} = 279.58$	$Ftg_{14} = 1268.69$
$atg_{15} = 10.51$	$Fcf_{15} = 206.37$	$Ftg_{15} = 936.48$
$atg_{16} = 10.17$	$Fcf_{16} = 156.94$	$Ftg_{16} = 712.19$
$atg_{17} = 10.17$	$Fcf_{17} = 51.791$	$Ftg_{17} = 235.025$

Determine the values of the following force projections on the axes:
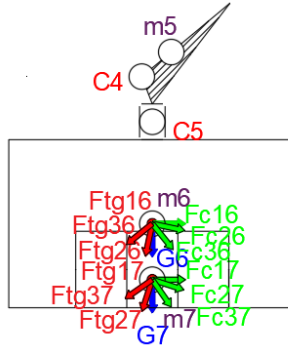
Figure 8. Representation of forces acting on the effector and the manipulated object.

•The projections of the forces acting on the effector (Figure 8) on the X-axis:

$$Fcf_{26}^x = Fcf_{26} \cdot cos(\alpha_{26} - 90°) \tag{50}$$
$$Fcf_{36}^x = Fcf_{36} \cdot cos(\alpha_{36}) \tag{51}$$
$$Ftg_{26}^x = Ftg_{26} \cdot cos(180° - \alpha_{26}) \tag{52}$$
$$Ftg_{36}^x = Ftg_{36} \cdot cos\,(180° - (90° + \alpha_{36})) \tag{53}$$
$$F_6^x = Fcf_{26}^x + Fcf_{36}^x + Ftg_{26}^x + Ftg_{36}^x + Fcf_{16}^x \tag{54}$$

•The projections of the forces acting on the manipulated object (Figure 8) on the X-axis:

$$Fcf_{27}^x = Fcf_{27} \cdot cos(\alpha_{27} - 90°) \tag{55}$$
$$Fcf_{37}^x = Fcf_{37} \cdot cos(\alpha_{37}) \tag{56}$$
$$Ftg_{27}^x = Ftg_{27} \cdot cos(180° - \alpha_{27}) \tag{57}$$
$$Ftg_{37}^x = Ftg_{37} \cdot cos(180° - (90° + \alpha_{37})) \tag{58}$$
$$F_7^x = Fcf_{27}^x + Fcf_{37}^x + Ftg_{27}^x + Ftg_{37}^x + Fcf_{17}^x \tag{59}$$
$$F_{RED}^X = F_6^x + F_7^x \tag{60}$$

•The projections of the forces acting on the effector (Figure 8) on the Z-axis:

$$Fcf_{26}^z = Fcf_{26} \cdot cos(\alpha_{26}) \tag{61}$$
$$Fcf_{36}^z = Fcf_{36} \cdot cos\,(90° - \alpha_{36}) \tag{62}$$
$$Ftg_{26}^z = Ftg_{26} \cdot cos\,(90° - \alpha_{26}) \tag{63}$$
$$Ftg_{36}^z = Ftg_{36} \cdot cos(\alpha_{36}) \tag{64}$$
$$F_6^z = Fcf_{26}^z - Fcf_{36}^z - Ftg_{26}^z - Ftg_{36}^z - G_6 \tag{65}$$
$$Fcf_{27}^z = Fcf_{27} \cdot cos(\alpha_{26}) \tag{66}$$
$$Fcf_{37}^z = Fcf_{37} \cdot cos\,(90° - \alpha_{36}) \tag{67}$$
$$Ftg_{27}^z = Ftg_{27} \cdot cos\,(90° - \alpha_{26}) \tag{68}$$
$$Ftg_{37}^z = Ftg_{37} \cdot cos(\alpha_{36}) \tag{69}$$
$$F_7^z = Fcf_{27}^z - Fcf_{37}^z - Ftg_{27}^z - Ftg_{37}^z - G_7 \tag{70}$$
$$F_{RED}^z = F_6^z + F_7^z \tag{71}$$

•The projections of the forces acting on the effector and on the manipulated object (Figure 8) on the Y-axis:

$$F_6^y = -Ftg_{16} \tag{72}$$
$$F_7^y = -Ftg_{17} \tag{73}$$
$$F_{RED}^y = F_6^y + F_7^y \tag{74}$$

Thus the forces acting on the effector and on the manipulated object were determined (Table 10).

Table 10. The values of forces actiong on the effector / manipulated object

Forces acting on X[N]	Forces acting on Z[N]	Forces acting on Y[N]
$Fcf_{26}^x = 135{,}88$	$Fcf_{26}^z = -28.88$	$F_6^y = -712.19$
$Fcf_{36}^x = 78.58$	$Fcf_{36}^z = 97.04$	$F_7^{zy} = -235.025$
$Ftg_{26}^x = 131.06$	$Ftg_{26}^z = 616.62$	$F_{RED}^y = -947.22$
$Ftg_{36}^x = 440.35$	$Ftg_{36}^z = 356.59$	
$F_6^x = 942.83$	$F_6^z = -1785.84$	
$Fcf_{27}^x = 44.84$	$Fcf_{27}^z = -9.806$	
$Fcf_{37}^x = 25.96$	$Fcf_{37}^z = 35.17$	
$Ftg_{27}^x = 66.11$	$Ftg_{27}^z = 209.27$	
$Ftg_{37}^x = 168.26$	$Ftg_{37}^z = 129.26$	
$F_7^x = 356.97$	$F_7^z = -610.14$	
$F_{RED}^X = 1299.81$	$F_{RED}^Z = -2395.98$	

Thus the axial (F_A) and radial (F_R) forces are:

$$F_A = F_{RED}^z \tag{75}$$
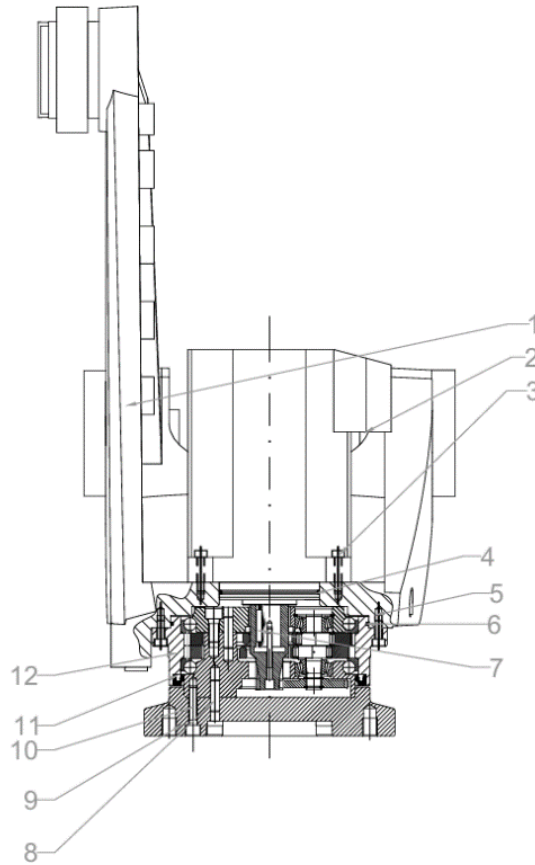
$$F_R = \sqrt{{F_{RED}^X}^2 + {F_{RED}^Y}^2} \tag{76}$$

The resulting moments resulting from the rotations in the pairs are:

$$M_{RED}^X = F_7^Y \cdot LG_7 \cdot 10^{-3} + F_6^Y \cdot LG_6 \cdot 10^{-3} \tag{77}$$
$$M_{RED}^Y = F_7^X \cdot LG_7 \cdot 10^{-3} + F_6^X \cdot LG_6 \cdot 10^{-3} \tag{78}$$
$$M_{REDUS} = 843.98 \, N \tag{79}$$

Following these calculations, the RV-40E gearbox from Nabtesco's catalog and the 9C1.1.60 actuator servomotor model, from ABB's catalog for numerically controlled axis 4 were chosen (Figure 9).

Figure 9. Sectional view of numerically controlled axis 4 where: 1 — ACN 4 housing; 2 — ACN 4 motor; 3— M6x30 screw; 4 — O-ring; 5— M6x20 screw; 6 — O-ring, 7 — Keyway; 8 — Threaded pin M8x20; 9 — Flange; 10 — M8x25 Screw; 11 — Shaft seal; 12 — RV-40E -105 Gearbox

Meanwhile, the calculus algorithm can also be employed for the same purpose in other IR models that have a similarly designed end-effector orientation subsystem.

4. Conclusion

This paper addresses two current approaches in the development of new pallet cells: the use of a prefabricated pallet cell and the design of a customized pallet cell optimized for the management of gravitational and inertial forces. It also lays the foundations for an improved model of a custom-designed palletizing cell tailored to optimize the kinematics of the structure **[7]**.

29

The second part of the paper focuses on a specialized algorithm developed for optimal motor selection in industrial robots used in palletizing applications. The detailed computational procedure presented in the paper is applied to various models of industrial robots, ensuring optimal motor selection, taking into account the gravitational and inertial forces inherent to palletizing operations. In addition, the applicability of the algorithm extends to similar robot models with comparable end-effector orientation subsystem designs. Rigorous testing of the proposed algorithm validated its effectiveness on several industrial robot models analyzed in this study.

References

1. G. Gamazeliuc, O. Ulerich, E. Rolea, M. Mărgăritescu, *Implementation of Human-Robot Interaction Through Hand Gesture Recognition Algorithms*, International Conference on Reliable Systems Engineering (ICoRSE) - 2023, D.D. Cioboată, Ed., Cham: Springer Nature Switzerland, 2023, pp. 147–154. doi: 10.1007/978-3-031-40628-7_12.
2. B.M. Verdete, C. Pupăză, G. Alexandru, Reduced order model for evaluating the temperature gradients of the surfacing weld process, *RRIA*, 33(1), pp. 7–20, Mar. 2023, doi: 10.33436/v33i1y202301.
3. IRB 660, M2004, Product specification. Accessed: Jul. 16, 2024. [Online]. Available: https://search.abb.com/library/Download.aspx?DocumentID=3HAC023932-001&LanguageCode=en&DocumentPartId=&Action=Launch
4. M.-A. Stamate, A.-F. Nicolescu, C. Pupază, Mathematical model of a multi-rotor drone prototype and calculation algorithm for motor selection, *Proceedings in Manufacturing Systems*, 12(3), 2017, pp. 119–128.

5. C.G. Coman, A.F. Nicolescu, C.A. Cristoiu, Calculus algorithm for evaluation of gravitational and inertial loads acting on a 6 dof articulated arm type industrial robot, *Proceedings in Manufacturing Systems*, 12(4), 2017, pp.187-194.
6. C. Dumitrașcu, F.A. Nicolescu, C.A. Cristoiu, Optimized overall design of a robotic arc welding cell and calculation procedures for optimal selection of ir motors, *Proceedings in Manufacturing Systems,* 16(2), 2021, pp. 75-88.
7. A.M. Ivan, A.F. Nicolescu, G.C. Avram, L Stan, Robotic deburring cell virtual prototyping, *Proceedings in Manufacturing Systems,*10(4), 2015, pp. 183-188.

Addresses:

- Roxana-Mariana Nechita, National Institute of Research and Development in Mechatronics and Measurement Technique, Bucharest, Romania
  roxana.nechita2000@gmail.com
  (*corresponding author*)
- Cozmin Cristoiu, National University of Science and Technology Politehnica Bucharest, Faculty of Industrial Engineering and Robotics, Bucharest, Romania, Cozzy Technologies SRL Pitesti, Romania
  cozmin.cristoiu@upb.ro
- Mihai Mărgăritescu, National Institute of Research and Development in Mechatronics and Measurement Technique, Bucharest, Romania,
  mihai.margaritescu@gmail.com